LC-DET-2001-080

A Lead Tungstate Detector with Integrated Light Readout for the TESLA Luminosity Calorimeter

H. M. Araújo[1], A. Stahl[2] and D. J. Miller[1]
[1] University College London, U.K.
[2] DESY/Zeuthen, Germany

Abstract

A lead tungstate calorimeter is proposed for the LCAL, the fast luminosity monitor of the TESLA detector. Scintillation light is detected by thin vacuum photodiodes placed between the crystals. Preliminary assessment of this technology indicates its suitability for luminosity studies. Monte Carlo simulations confirm that the intrinsic performance of the proposed design does not compromise the accuracy of physics measurements which could be made in this region, though uncertainties in the subtraction of the beamstrahlung background will limit what can be achieved. Several issues requiring further study are pointed out.

1 LCAL, the Luminosity Calorimeter

The requirements of the LCAL and a possible baseline design have been discussed in the TESLA TDR [1]. This provides the framework for the ideas reported in this note.

Fast monitoring of the luminosity in the very forward region of the TESLA detector will rely on the measurement of large numbers of e^+e^- pairs produced after beamstrahlung near the interaction point (IP). Beamstrahlung photons are produced in the coherent electromagnetic field of opposing beam bunches by synchrotron emission. A fraction of these are converted into e^+e^- pairs, which spiral along the magnetic field in the $\pm z$ direction. A significant number of these particles hits the LCAL ($\sim 10^4$/BX), depositing over 20 TeV in each detector.

The total energy, the energy spectrum and the spatial distribution of these soft pairs carry valuable information on the colliding beams, such as the beam overlap at the interaction region and, to first approximation, the total luminosity. Some of these parameters can then be fed back to the beam delivery system (BDS), either on a 1 BX timescale or after more complex processing, in order to help maximise luminosity.

Simultaneously, the LCAL must complement the hermeticity of the end-cap region of the detector, a matter of considerable importance to the physics studies to be conducted at the Linear Collider. These goals translate into quite demanding performance targets: the LCAL must survive and measure the multi-TeV pair background on a time-scale shorter than the interbunch spacing (176 ns for a 800 GeV machine) and still be able to identify (tag or veto) electrons in the energy range $\sim$100–400 GeV, with acceptable energy and spatial resolutions. Ultimately, the ability to measure a physics signature is determined by how effectively the beam-induced background can be subtracted. It is important, therefore, that the intrinsic performance of the detector does not compromise the overall accuracy of the measurement.

A device installed around the beam-pipe, inside the instrumented tungsten mask, will also play an important role in shielding the main detector from backscattered pairs, neutrons and synchrotron radiation. In the TDR this function is complemented by a 10-cm thick ($\simeq 0.5\ X_0$) graphite plate placed in front of the LCAL to prevent backscattering of the low energy pairs.

Further to these requirements, other constraints apply to a detector operating in this very forward region ($\theta \lesssim 30$ mrad). Its location inside the tungsten mask imposes limits to the size and accessibility of the system, so that it should be compact and reliable over the lifetime of TESLA. Also, it must operate inside a large (4 T) magnetic field.

1.1 Candidate technologies

Two technologies already proposed for the LCAL were Si/W and diamond/W sampling calorimeters. Both deliver good performance in terms of energy and spatial resolution, as well as speed (see Section 3.5.2, p. IV-89 in [1]).

A calorimeter based on pure silicon would not withstand the doses anticipated for 10 years of TESLA operation (~ 10 MGy). Oxygenated silicon, which has been developed by the RD48 (ROSE) collaboration and successfully transferred to the LHC and industry, is better suited: it does not undergo type inversion at least up to doses of 4 MGy, although some cooling (-10^{o}C or lower) is required to deal with the large increase in leakage current expected upon irradiation [2]. Pure silicon becomes radiation hard at temperatures below $\simeq 100$ K — the so-called Lazarus effect — but this would require more awkward arrangements for cryogenic equipment.

Diamond is radiation hard up to the required doses, and such a detector would not need replacement for the lifetime of TESLA [3]. However, its cost (a factor of ~ 200 over silicon) makes this a less attractive proposal, even in a mixed configuration with Si/W.

A lead tungstate (PWO) scintillator calorimeter has also been proposed in which light is read out by optical fibres coupling the scintillator crystals to multi-channel photomultiplier tubes (PMT) located outside the TESLA detector [4]. This is a feasible solution, although not a straightforward one to implement. Coupling scintillation light to optical fibres is notoriously difficult (especially with small crystals) and the need to observe a minimum fibre bending radius inside a relatively fine granularity complicates matters further.

The alternative described here is to readout the scintillation light *in situ* between the longitudinal layers of the calorimeter. We propose to accomplish this by means of vacuum photodiodes (VPDs) just a few millimetres thick, placed directly behind the lead tungstate crystals. The underlying idea is to trade off readout gain (the VPD has no gain) for a much better coupling efficiency for scintillation photons.

To be directly embedded in this region of the TESLA detector, a photon detector must fulfil stringent requirements with respect to radiation hardness, insensitivity to magnetic fields, the nuclear counter effect (signal from direct hits by radiation) and size. This excludes common solid-state technologies, such as silicon avalanche photodiodes, as well as larger vacuum tubes. Flat vacuum photodiodes could overcome these shortcomings.

2 An integrated PWO crystal calorimeter

The geometry discussed in this note is that represented in Fig. 1. It has cylindrical symmetry and is non-projective towards the IP (the front face of the detector is ~ 2 m away from the interaction region). The calorimeter would be segmented into 6 *slices* in the longitudinal (z) direction, each 4 cm thick and separated by gaps of 1 cm. Each slice is divided into 7 *rings* 1 cm thick, between radii $r = 1.2$ cm and $r = 8.2$ cm. The outer edge of the detector is extended by a further Moliere radius relative to the radial acceptance (corresponding to the out-most two rings) in order to improve shower containment. Azimuthal *wedges* span an angle $\Delta\phi = 15^{o}$.

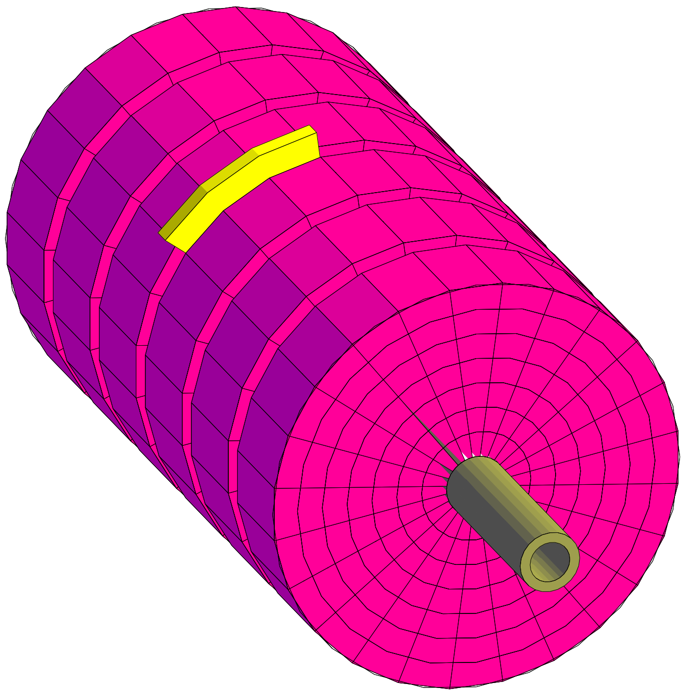

Figure 1: Crystal layout for the cylindrical, non-projective geometry. Also shown is the placement of one of a total of 48 multi-channel VPDs, each 5 mm-thick and spanning an angle of 45^o. The innermost 5 rings correspond to the unobstructed acceptance region.

The scintillation light is detected by wedge-shaped vacuum photodiodes placed behind each slice. In the following it is assumed that each VPD reads all crystals for each 3 sectors in ϕ (21 channels), all individually connected to low-noise, fast amplifiers located in the vicinity of the detector. Alternatively, the azimuthal segmentation could vary with radius as shown in Fig. 2 a) for easier fabrication of the readout devices.

A rectangular geometry has also been looked at, as a less demanding alternative in terms of crystal and photodiode shapes. In this rectangular layout each slice is segmented into arrays of 15$\times$15 crystals, each 1 cm^2 in cross-section. The scintillation is detected by 3$\times$3-channel photodiodes, such as that shown in Fig. 2 b).

The choice of granularity for both geometries is guided by the following factors. The fine transverse segmentation ($\sim 0.5 R_M$) helps to measure the distribution of the pair background in the r–ϕ plane. This is an important feature for luminosity studies, besides helping to distinguish between background particles and electrons near full beam energy.

Electron identification is better accomplished by longitudinal segmentation, since the softer pairs shower slightly earlier than higher energy particles — though the depth of shower maximum increases only logarithmically with energy. In PWO shower maxima occur at less than $6X_0$ for energies lower than 10 GeV (which includes the overwhelming majority of background particles), whereas the shower of a 250 GeV electron peaks at about $9X_0$. Therefore, the ratio of the energy deposited by signal electrons to the pairs increases towards the back of the calorimeter. Information on longitudinal shower development is also needed to distinguish backscattered particles which enter the calorimeter from the back.

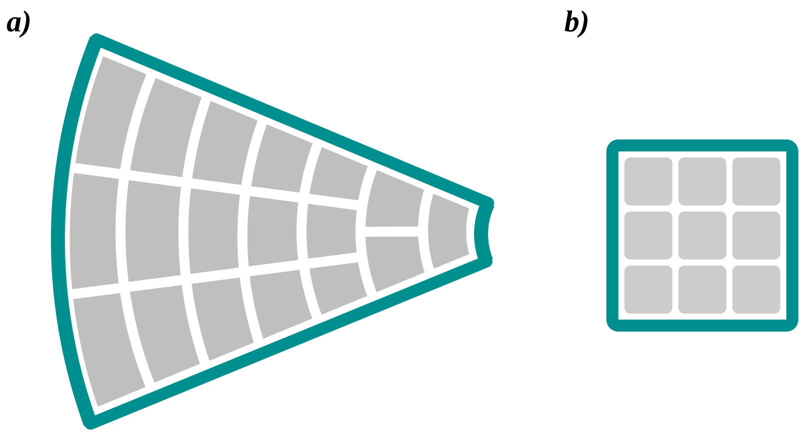

Figure 2: Schematic representation of multichannel vacuum photodiodes; a) A possible 45° diode for the cylindrical geometry in Fig. 1; (b) 3×3-channel diode for the rectangular geometry.

2.1 The lead tungstate scintillator

Lead tungstate, $PbWO_4$, is amongst the densest scintillators know, with a radiation length $X_0 = 0.89$ cm and a Moliere radius $R_M = 2.2$ cm. In spite of a relatively low light output ($< 1\%$ NaI) other characteristics, such as speed and radiation hardness, make it a very appealing material for high energy physics experiments.

The scintillation properties of PWO have improved significantly in recent years, owing mainly to the efforts of the CMS collaboration to improve its light yield, radiation hardness, speed, uniformity of light collection and reproducibility of crystal properties. CMS endcap pre-production crystals have achieved — even surpassed — the stringent targets originally set out. The final pre-production batches demonstrated $\simeq 70\%$ longitudinal transmission at 420 nm (goal 55%), a light yield (LY) just above 10 phe/MeV (goal 8 phe), and a LY loss after low dose rate irradiation saturating at just $\simeq 2.5\%$ (goal 6%) [5, 6]. The material specifically doped for improved radiation hardness has an average decay time constant of 15 ns, and a scintillation spectrum extending from 360 nm to 570 nm ($> 10\%$ of peak).

In this note a modest LY of 10 phe/MeV has been adopted, already achieved for the much larger CMS pre-production crystals. As many as 16 phe/MeV can be extracted from 1 cm^3 CMS test crystals optimised for radiation hardness, and higher values can be obtained for crystals specifically doped for increased light collection [7].

The materials providing the stopping power in the LCAL will have to endure electromagnetic doses of up to 10 MGy over 10 years of operation. Furthermore, neutron fluxes of the order of 10^{13} 1 MeV n/cm^2/year are expected [8, 9]. The effects of high-dose irradiation in PWO are relatively well understood (see, for example, [10, 11]). Both photon and neutron irradiation affect the optical transmission of the crystal, but not the scintillation mechanism itself. For the best CMS crystals, the loss in LY saturates at a few percent for doses above ~ 10 Gy, as irradiation causes an increase in the absorption coefficient at peak emission by $\Delta\kappa \simeq 0.4$ m^{-1}. PWO has been tested only up to 100 kGy by the CMS Crystal Clear collaboration. No deviation from the low-dose saturation behaviour has been observed for gamma rays, or indeed with MeV neutron fluences up to 10^{13} n/cm^2.

Optical properties recover noticeably over timescales of 1 hour, and many crystals recover fully in ~ 1 day. To allow for normal beam-off periods of a few hours, crystals with higher LY loss may be selected, since these take longer to recover. For example, the first signs of recovery in crystals exhibiting a 20% LY loss should appear only after several hours.

In case some light can be sacrificed, optical filtering can help to cope with radiation-induced variations in LY. Filtering out the blue part of the scintillation spectrum reduces the sensitivity to irradiation as $\Delta\kappa$ is smaller at longer wavelengths.

2.2 Light readout

We envisage a segmented anode or photocathode with the kind of channel layout depicted in Fig. 2. Signals can be fed through the VPD envelope for example into a printed-circuit board, common to a whole slice, patterned with microstrip transmission lines. Bialkali photocathodes should provide quantum efficiencies $> 20\%$ over most of the scintillation spectrum of PWO. This figure could be improved on by recoupling single-pass transmission losses with a reflection coating at the back of the device.

Vacuum photodiodes 5 mm thick, akin to those proposed here, have recently been considered in order to provide longitudinal sampling in a Shashlik calorimeter [12, 13]. However, the LCAL readout is a more challenging application, namely in terms of radiation hardness and fabrication of a multichannel device.

The radiation-induced effects that could compromise the operation of VPDs or limit their lifetime can be divided into two categories. Firstly, one must consider the issue of radiation hardness of both the photocathode and the glass envelope. The resistance of photocathode materials to high-dose irradiation is currently being investigated, for example in the frame of LHC detectors. Bialkali photocathodes are not expected to be seriously affected due to their amorphous structure. On the other hand, borosilicate glasses are known to suffer damage when exposed to electromagnetic radiation or neutrons, becoming dark at relatively low doses. Other potential problems are activation of the window material (phosphorescence) and insulation failure. A quartz-window PMT with standard bialkali photocathode has been found to survive high doses (1 MGy) with no significant damage (see [14] and references therein). Optical-fibre Cherenkov calorimeters have motivated recent studies of quartz fibres irradiated to high doses. Tests with 500 MeV electrons up to a dose of 1 MGy reveal a radiation-induced absorption below 10 dB/m over the emission spectrum of PWO [15]. Although composition and fabrication technology are important factors, quartz windows ~ 1 mm thick are not expected to be greatly affected.

The second category includes nuclear counter effects (radiation-induced pulses), which can arise from Cherenkov radiation and scintillation in the glass envelope as well as direct hits in the photocathode. These should be unimportant compared to the optical signal.

VPDs easily meet the speed requirement (phe transit times ~ 1 ns), which is instead determined by the amplifier. Low capacitance, linearity of response and large dynamic range are also intrinsic features. Operation in the large magnetic field is not problematic; in fact, a field perpendicular to the photocathode will provide a focusing effect for photoelectrons and help reducing crosstalk.

The readout noise has contributions from both the amplifier and the diode — the latter through its leakage current (shot noise) and the capacitance presented to the amplifier input. The combined capacitance of a 1 cm^2 VPD channel and a 10-cm long transmission line should be as low as 10 pF. Due to the low bias voltage required (10–20 V), the leakage current through the VPD envelope can be kept very low.

Fast, radhard amplifiers, such as the SCTA chip developed for the ATLAS Central Tracker, can achieve noise figures of ENC ~ 1000 e$^-$ with a shaping time of 25 ns for low capacitance loads [16]. These could be mounted inside the tungsten mask, around the LCAL, thus keeping cable capacitance to a minimum. In terms of minimum ionising particles (mip), ENC $\simeq 2$ mip for our crystals, using a collision stopping power $(1/\rho)dE/dx \approx 1.5$ MeV cm^2/g [17].

3 Performance for electron tagging

3.1 The beam-induced background

Subtraction of the pair background will ultimately set the accuracy for electron tagging in the LCAL. In this respect, two aspects must be considered, namely the characteristics of an individual 'background event' (1 BX) and the stability on a bunch-to-bunch basis.

Beamstrahlung events calculated with GUINEA-PIG [18] have revealed some important characteristics. For example, the positrons are focused by the oncoming electron beam as they travel along the magnetic field in the $+z$, most disappearing inside the beam pipe, while the electrons are defocused, many hitting the LCAL. The roles are reversed for the $-z$ direction.

The spatial distribution of electrons and positrons is shown in Fig. 3 a) for one background event with typical machine settings. A slight departure from the cylindrical symmetry to a more oblong shape is observed inside the acceptance region, which contains mostly electrons. Fig. 3 b) represents the energy spectrum inside the radial acceptance (in front of the graphite layer) for the $+z$ detector. The total energy contained in the acceptance region approaches 40 TeV for this particular event.

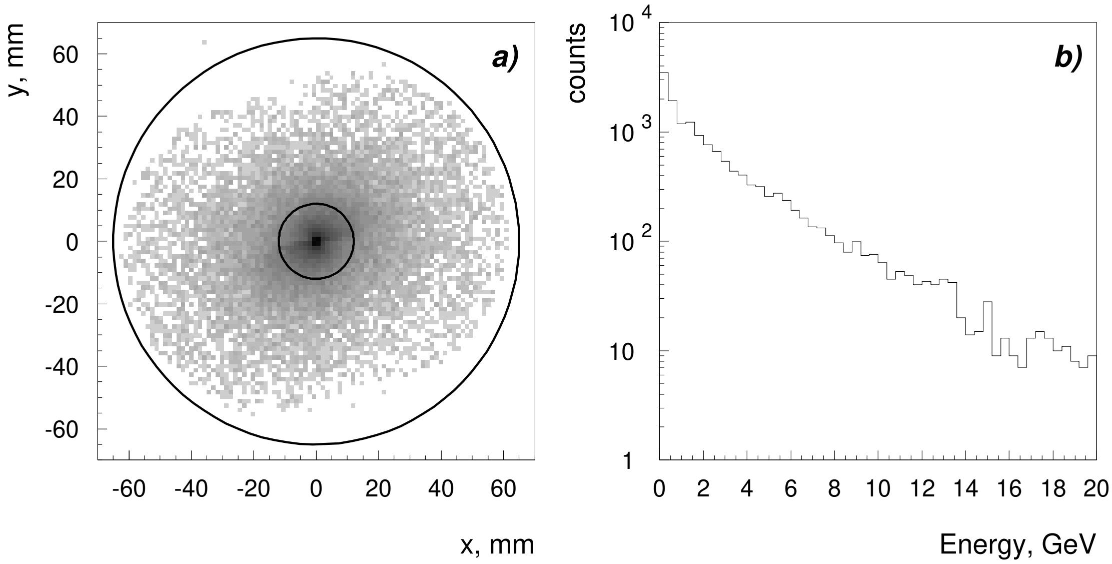

Figure 3: Background event calculated with GUINEA-PIG [18]; a) Spatial distribution of particles hitting the graphite layer in front of the $+z$ LCAL (log scale); the circles mark the radial acceptance of the detector. b) Energy spectrum of the preceding event within the radial acceptance.

The number of background pairs is loosely proportional to the total luminosity, so the question is how much will the latter fluctuate from one bunch to the next. The fast feedback system is the component of the BDS with the task of correcting for the beam-beam separation and collision angle at the IP on the timescale of a few bunch crossings. The nominal goals for the fast feedback system are the control of the beam offset to $\Delta y < 0.1\sigma_y$, where $\sigma_y \simeq 5$ nm is the vertical size of the beam, and the beam tilt to $\Delta y' < 0.1\sigma_{y'}$, where $\sigma_{y'}$ is the vertical crossing angle. These targets translate into luminosity fluctuations — and hence background fluctuations — of around 10% (Section 7.3, p. II-184 in [1]).

The spatial characteristics of an individual event in one detector can be used in the background subtraction, provided they are well defined and understood. For example, the azimuthal symmetry can be exploited by subtracting the signals from radially opposing crystals. Another possibility is to subtract the background from the preceding bunch crossing. These two methods have been analysed in [19] for a crystal layout similar to ours, and found to work equally well for the particular background parameters and fluctuations assumed there. An efficiency above 80% was found for identifying 250 GeV electrons, decreasing to about 63% for 100 GeV electrons.

Somewhat better accuracy could be obtained by subtracting an average of a number of preceding backgrounds, if their shape and energy fluctuate by only a small amount around some equilibrium configuration, and as long as the number of signal events is relatively small.

The number of background events to average is limited by the rate of signal events. Elastic Bhabha scattering is particularly important in the angular region of the LCAL, where an event rate of $\simeq 6500/\mathrm{s}$ is expected at $\sqrt{s} = 500$ GeV and $\mathcal{L} = 3.4 \times 10^{34}\ \mathrm{cm}^{-2}\mathrm{s}^{-1}$ (less than 1 event/100 BX). Tagged $\gamma\gamma$ events hit the LCAL at comparable rates and their signatures also consist of electrons near full beam energy. Untagged $\gamma\gamma$ events lead to hadronic interactions in the calorimeter, which are less likely to upset signal identification since their showers will be of lower energy and spread over more crystals.

Once the BDS 'locks' at peak luminosity, averaging N background events can reduce the statistical fluctuations in the subtraction by a factor $\sqrt{2/(1+1/N)}$, i.e. a maximum improvement of $\simeq 40\%$. It should be noted, however, that the feedback corrections may operate on timescales of up to $\sim$100 bunch crossings, depending on the disruption from equilibrium, which can compromise the averaging for the initial 3% of each bunch train.

In the following we concentrate on the intrinsic performance of the detector to measure electrons near full beam energy, leaving aside the pair background, but keeping in mind that it may fluctuate by as much as 10% per bunch crossing.

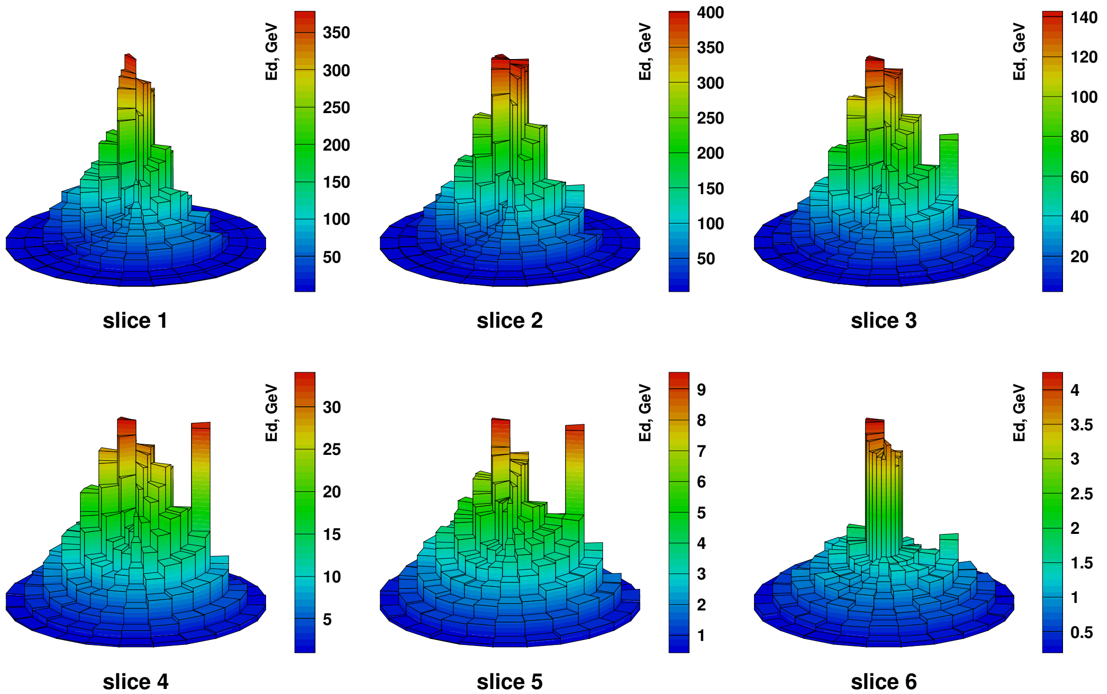

Figure 4: Energy deposited in the calorimeter crystals by the pair background of 1 BX plus a 250 GeV electron at r=4.7 cm (visible, for example, on the right hand side of slice 4).

3.2 Energy resolution

The cylindrical layout represented in Fig. 1 was simulated using Geant4. A range cut of 50 μm was applied to PWO crystals, corresponding to production thresholds of $\sim$ 10 keV for electrons and $\sim$ 100 keV for gammas. The energy deposited in each crystal by the background event just described is shown in Fig. 4. The signal from a 250 GeV electron entering the detector at $r = 4.7$ cm is also shown for comparison. Although the electron is clearly seen in slices 3–6, one should note its large energy and favorably outward position (4th ring out of 6 possible for direct hits). It is also apparent that the pair background fires nearly every channel in the LCAL every bunch crossing!

Good containment of the background is important to prevent particles leaking back to the main detector. The longitudinal gaps between slices have little effect on the total energy deposited in the calorimeter. The typical background event deposits 89.8% of the total energy in the acceptance region without such gaps; this figure decreases by 1% for 5 mm gaps and by a further 1% for the 10 mm gaps considered here.

The average fraction of energy deposited by electrons of energy E in several parts of the calorimeter (E_d/E) is shown in Fig. 5 a). A readout threshold $E_{th} = 0.5$ GeV is applied to all crystals. Electrons are fired horizontally at the middle of a crystal in the inner ring (r=1.7 cm), the 4th ring (4.7 cm) and near the outer radial acceptance (6.2 cm).

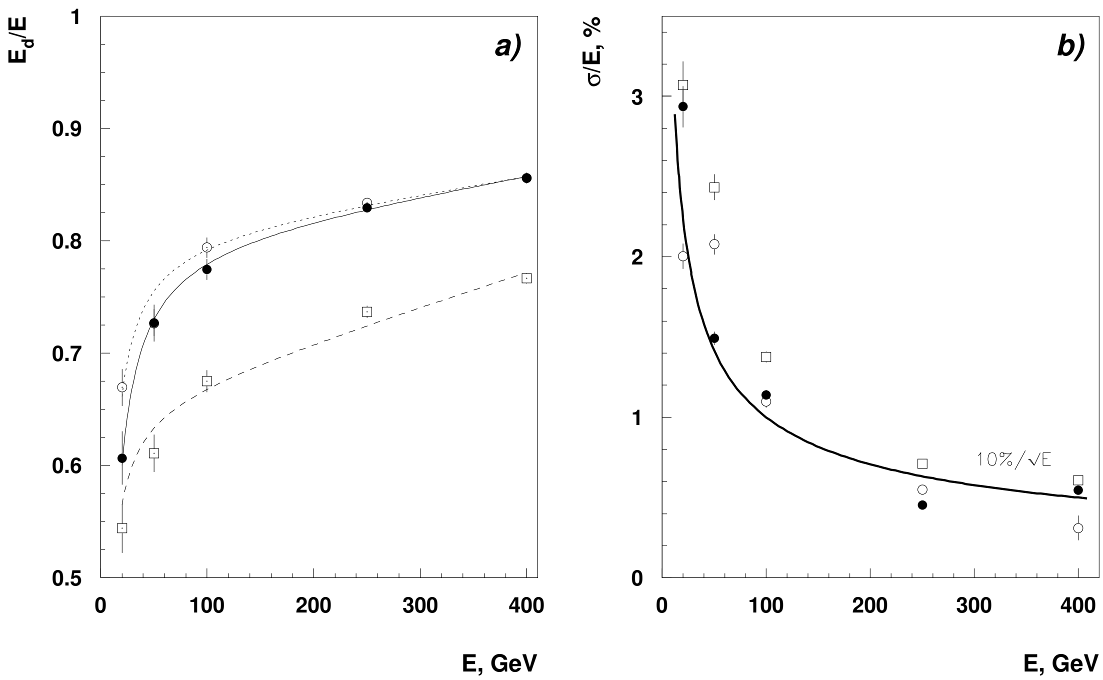

Figure 5: a) Fraction of energy deposited in the calorimeter above a crystal threshold E_{th} = 0.5 GeV, at r=1.7 cm (□), r=4.7 cm (•) and r=6.2 cm (∘). b) Contribution of shower fluctuations to the stochastic term in Eq. 1, referred to the particle energy E; the line represents a $10\%/\sqrt{E}$ dependency.

The energy resolution, σ, of a calorimeter is usually written in the form:

$$\frac{\sigma}{E} = \frac{a}{\sqrt{E}} \oplus b \oplus \frac{c}{E}, \qquad (1)$$

where a is the stochastic term, b is the constant term and c is the noise term.

The stochastic term is dominated by shower sampling fluctuations, which are shown in Fig. 5 b). This term has a value of $\simeq 10\%/\sqrt{E}$ at the centre of the acceptance region, rising to $\simeq 13\%/\sqrt{E}$ at the middle of the inner ring. Photoelectron statistics adds a contribution $\sigma/E = \sqrt{1/LE}$, where L is the photoelectron yield per GeV ($L = 10^4$ phe/GeV). This term is small ($1\%/\sqrt{E}$) due to the efficient coupling that can be achieved with thin VPDs.

Crystal calorimeters are affected much less by shower fluctuations than sampling calorimeters, but this is only advantageous if the constant term can be kept small ($b <$ 0.5%). The latter is due to shower leakage and non-uniformity of the light collection along the crystal, and is difficult to estimate by simulation alone. Here we assume $b = 0.5\%$.

The noise term, c, is mainly due to amplifier noise. For a number n of channels read per event, the amplifier noise contribution is $\sigma/E = \sqrt{n}\,E_N/E$, where $E_N = \mathrm{ENC}/L \sim$ 0.1 GeV is the noise level for an amplifier with ENC = 1000 e$^-$. If all $\sim$ 1000 channels were to be read, then $\sigma/E \simeq 300\%/E$, for E in GeV.

The need to impose a high readout threshold is thus clear. A fixed threshold $E_{th} =$ 0.5 GeV ($=5E_N$) results in a negligible probability of any channel firing accidentally, and reduces the number of channels considerably (to about 40 for 250 GeV electrons, for example). The simulation shows the general trend $n \simeq 0.6E^{3/4}$, which leads to a noise term $\sigma/E \simeq 8\%/E^{5/8}$. Nevertheless, one should bear in mind that the overwhelming pair background will still fire nearly all channels in the LCAL. Larger thresholds, perhaps varying for each slice, should be considered. A dual readout, consisting of both fast amplifiers for luminosity studies and a slower, less-noisy readout for signal events is also a possibility.

The *intrinsic* (no background) energy resolution thus estimated for this calorimeter can be summarised in the form:

$$\frac{\sigma}{E} = \frac{[9.6-12.9]\% \oplus 1\%}{\sqrt{E}} \oplus 0.5\% \oplus \frac{8\%}{E^{5/8}}, \tag{2}$$

for E in GeV. The breakdown of the various contributions to σ/E is shown in Fig. 6. A value $\sigma/E \simeq 1\%$ is expected above 250 GeV, although this figure will almost double if all channels have to be read. In any case, an intrinsic resolution at the 1% level is expected to be smaller than the uncertainty introduced by the beam-induced background.

3.3 Position reconstruction

The statistical uncertainty in the reconstruction of the spatial coordinates was estimated for 250 GeV electrons entering the calorimeter perpendicularly to the r–ϕ plane. Other factors that contribute to the true position resolution of the detector have been left out, namely those associated with the light readout, gain variations in the amplifiers, mechanical (metrology) effects and the beamstrahlung signal. However, this provides a useful figure of merit.

Several systematic effects associated with energy fluctuations bias the position reconstruction of the shower axis. One is related to the efficiency for shower containment in the r–ϕ plane. These edge effects are complicated by their variation along z. The magnetic field affects the reconstruction of the azimuthal coordinate in a similar way.

Another bias is introduced by the reconstruction algorithm near crystal boundaries, and therefore has a spatial period equal to the crystal size. In order to minimise this effect, the choice of algorithm must take into account how the lateral shower dimensions compare to the transverse granularity. We assume that all systematic effects are perfectly corrected for, and concentrate only on statistical fluctuations.

Only slices 2–5 have been used in the reconstruction; as shown in Fig. 4, the first slice is completely overwhelmed by the pair background, while the last one is too close to the readout threshold.

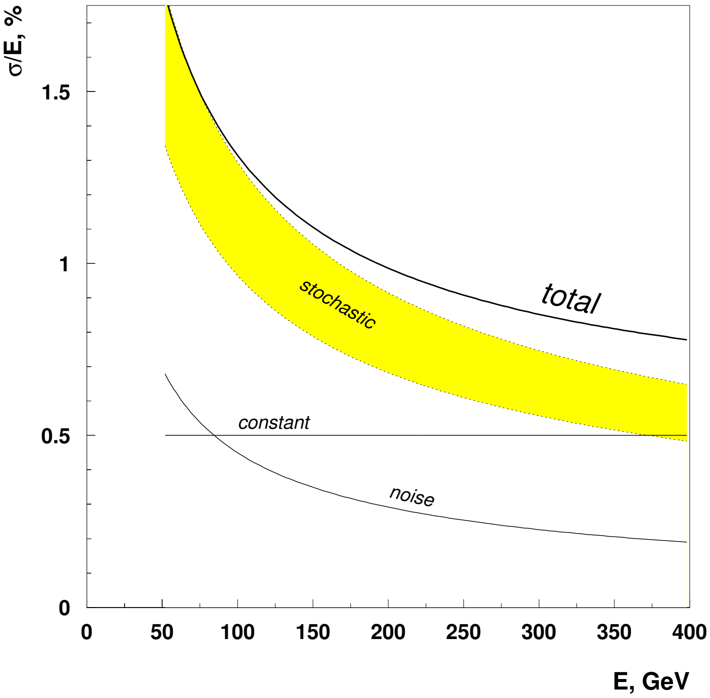

Figure 6: Energy resolution for $E_{th} = 5E_N$. The shaded area represents the variation of the stochastic term with the radial coordinate; the curve labelled 'total' is calculated for an intermediate stochastic term.

The radial and azimuthal coordinates are reconstructed with the following simple recipe. Firstly, the pixel with maximum energy deposition is identified for each slice. A correction for crystal volume is then applied for the two adjacent neighbours in r. A simple 3-pixel centroid is calculated when the ratio of the peak to the two adjacent neighbours is above a certain value (3, in this case). Otherwise, only the ratio of the peak to the highest neighbouring channel is used.

The *rms* uncertainty in r is found to remain fairly constant for all rings: $\sigma_r \simeq 150\ \mu$m at pixel boundaries, improving by a factor of approximately 3 near the pixel centres. The uncertainty in the polar angle is therefore $\sigma_\theta < 1$ mrad over the whole acceptance region. The *rms* uncertainty in ϕ is also at the level of 1% of the pixel dimension: $\sigma_\phi \simeq 0.2$ degrees.

These figures indicate that the contribution of random shower fluctuations to the position resolution of a PWO detector is comparable to that expected for a Si/W sampling calorimeter. Although systematic effects, some of which have been pointed out above, are much more severe for the crystal calorimeter, the uncertainty introduced by the pair background is again likely to dominate for both technologies.

4 Future work

Further studies into a number of issues are in order, either specifically related to R&D on a PWO detector, or more generally to understand the workings of the machine/detector interface. Firstly, it is essential to define unambiguously both the physics and the luminosity studies that are envisaged for the polar angles covered by the LCAL. More complete simulations of the beam-induced background would also be welcome, using realistic machine parameters which take into account internal bunch deformations (e.g. the 'banana' effect). Beamstrahlung studies should extend to lower energies, for example closer to the Z^0 production threshold.

Once a working concept has been decided upon, it is important to define exactly how this will interact with both the TESLA detector and the accelerator. Integration into the feedback mechanism in the BDS, data acquisition, metrology and mechanical feasibility are aspects that require further attention.

Very few studies exist on the radiation hardness of materials and devices up to electromagnetic doses as high as those considered here. Taking an upper value of 1 TeV/BX for the maximum energy deposited per crystal, easily achieved in a 800 GeV machine, we estimate a dose of 10 MGy in PWO over 10 years of TESLA operation. However, the irradiation studies conducted in the frame of the CMS experiment have fallen short of this value by two orders of magnitude. The effect of high energy neutrons also needs to be explored. Testing VPDs under heavy irradiation is also required. Again, the doses expected for quartz ($\simeq 1/3$ of PWO) are higher than those reached in existing studies of vacuum tubes.

The dynamics of damage saturation and recovery in PWO must be analysed with TESLA characteristics in mind. The effect of radiation annealing of individual crystals on the overall performance of the LCAL should be simulated in detail, including the past history of each crystal according to its location, machine parameters and damage/recovery timescales. This is well illustrated by Fig. 4: the LY loss of a crystal located in the inner ring of the first slice may saturate in a matter of minutes, while those further out and back may take weeks to reach a dose of 10 Gy. Such study may highlight the need to develop a system for monitoring the optical absorption, for example between the 5 Hz TESLA trains. The extent to which thermal stabilisation is required also needs to be investigated.

Thin VPDs have been prototyped in the past. However, we propose a more challenging design. Issues to be explored with the manufacturers include photocathode technology. Bialkali photocathodes have higher sensitivity and are expected to be less prone to damage by irradiation. However, it is unlikely that they can be deposited in place, as in larger phototubes, which complicates their fabrication significantly. Also, integration of a quartz window, or other boron-free glass, in the VPD envelope must be investigated.

Readout noise will dominate the intrinsic performance of this PWO calorimeter. Maximising the light yield and reducing amplifier noise must be a priority. Implementation of a dual readout scheme should also be explored.

Finally, the results discussed here could improve if a new, denser scintillator could be developed which is also fast and radiation hard. This search is ongoing, motivated by both high energy physics and medical applications.

5 Conclusions

An alternative technology is proposed for the TESLA luminosity calorimeter (LCAL), consisting of a lead tungstate scintillation detector with integrated light readout using thin vacuum photodiodes. The assessment reported in this note indicates that this solution is expected to compete favorably with others already proposed for that system in terms of intrinsic performance and cost. Further studies are required, namely on the radiation hardness of PWO and the readout devices up to the very high doses anticipated.

Acknowledgments

We would like to thank the following people for valuable discussions and information: T. Behnke and K. Büßer (DESY/Hamburg), P. Hobson (Brunel University, UK), P. Lecoq

(CERN EP/CMA), P. Checchia (INFN/Padova) and A. Howard (Imperial College, UK). H. Araújo acknowledges travel support from the INTAS 00-00679 project.

References

[1] *TESLA Technical Design Report*, DESY-2001-011, ECFA-2001-209, 2001.

[2] G. Lindström *et al.*, *Radiation hard silicon detectors — developments by the RD48(ROSE) collaboration*, Nucl. Instr. Meth. A466, pp. 308–326, 2001.

[3] T. Behnke *et al.*, *Electromagnetic Radiation Hardness of Diamond Detectors*, hep-ex/0108038, DESY-2001-117, 2001.

[4] Uriel Nauenberg, University of Colorado, private communication.

[5] P. Lecoq, *Status of New technology Development in Bogoroditsk*, CMS Week, Catania, June 2001. (Available at hepwww.rl.ac.uk/CMSecal/Crystals/).

[6] E. Auffray, *First results on the 100 R&D crystals measured in RCCERN on ACCOCE2*, CERN EP-CMA, 2001. (Available at hepwww.rl.ac.uk/CMSecal/Crystals/)

[7] A. Annenkov *et al.*, *Improved light yield of lead tungstate scintillators*, Nucl. Instr. Meth. A450, pp. 71–74, 2000.

[8] G. Wagner, *Neutron Background Studies at the TESLA Collider*, LC-DET-2001-048, 2001.

[9] K. Büßer, *Beam induced backgrounds at TESLA*, First Workshop of the Extended ECFA/ DESY Study "Physics and Detectors for a 90 to 800 GeV Linear Collider", Krakow, Poland, Sept. 14–18, 2001. (available at fatcat.ifj.edu.pl/ecfadesy-krakow/talk.php?tid=112).

[10] A. Annenkov *et al.*, *On the origin of the transmission damage in lead tungstate crystals under irradiation*, CMS-NOTE-1998-041, 1998.

[11] E. G. Devitsin *et al.*, *Non-stoichiometric Defects and Radiation Hardness of Lead Tungstate Crystals $PbWO_4$*, CMS-CR-2001-013, 2001.

[12] A. C. Benvenuti *et al.*, *Testbeam results for a Shashlik calorimeter with longitudinal segmentation*, Nucl. Phys. B (Proc. Suppl.) 78, pp. 226–231, 1999.

[13] P. Checchia, *A Shashlik e.m. Calorimeter with Longitudinal Segmentation for a Linear Collider Experiment*, Linear Collider Workshop 2000 – LCWS 2000, Fermilab, October 2000.

[14] Chapter 8 in *HCAL Technical Design Report*, CERN/LHCC 97-31, CMS TDR 2, 1997. (available at uscms.fnal.gov/uscms/Subsystems/HCAL/hcal_tdr/ch08/)

[15] I. Dumanoglu *et al.*, *Radiation-hardness Studies of High OH^- Content Quartz Fibers Irradiated with 500 MeV Electrons at CERN*, CMS-NOTE-2001-020, 2001.

[16] F. Anghinolfi *et al.*, *SCTA - A Rad-Hard BiCMOS Analogue Readout ASIC for the ATLAS Semiconductor Tracker*, 1996 IEEE Nuclear Science Symposium, Anaheim, CA, Nov 1996, Ed. A. Del Guerra, pp. 46–50, 1997. (reprint CERN-ECP-96-016).

[17] F. Gautheron and A. Givernaud, *About the electromagnetic shower lateral profile in the lead tungstate*, CMS-NOTE-1997-037, 1997.

[18] D. Schulte, *Beam-beam simulations with GUINEA-PIG*, CERN-PS-99-14, CERN-CLIC-NOTE-387, 1999.

[19] A. Stahl, *Investigations into electron-ID with LCAL*, First Workshop of the Extended ECFA/DESY Study "Physics and Detectors for a 90 to 800 GeV Linear Collider", Krakow, Poland, Sept. 14–18, 2001. (available at fatcat.ifj.edu.pl/ecfadesy-krakow/talk.php?tid=62).